Article | Open Access

Energy Materials

Zhang *et al. Energy Mater.* **2026**, *6*, 600109 **DOI:**10.20517/energymater.2026.184

Reconstruction-mediated interfacial water engineering in Cu-Mo electrocatalyst for highly efficient and durable water splitting

Jianfang Zhang[1,2,#], Jiapei Li[2,#], Yan Wang[1,*], Miao Han[1], Chuhao Luan[2], Shuai Xia[1], Cuiping Yu[1], Yucheng Wu[1,3,*], Wenjun Zhang[2,*]

Keywords:
Catalyst reconstruction, interfacial water, hydrogen evolution reaction, oxygen evolution reaction, water splitting

Citation: Zhang, J.; Li, J.; Wang, Y.; Han, M.; Luan, C.; Xia, S.; Yu, C.; Wu, Y.; Zhang, W. Reconstruction-mediated interfacial water engineering in Cu-Mo electrocatalyst for highly efficient and durable water splitting. *Energy Mater.* **2026**, *6*, 600109. https://dx.doi.org/10.20517/energymater.2026.184

Received: 24 Jun 2026
First Decision: 16 Jul 2026
Revised: 20 Jul 2026
Accepted: 3 Aug 2026
Published: 27 Aug 2026

Academic Editors:
Yuping Wu, Qi-Long Zhu
Copy Editor:
Fangling Lan
Production Editor:
Fangling Lan

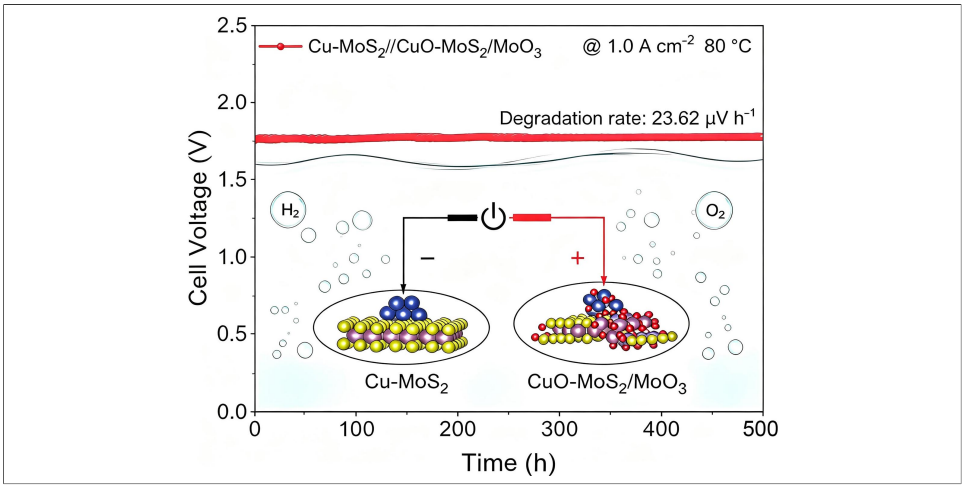

Abstract

The development of efficient and durable electrocatalysts for industrial-level water splitting remains a critical challenge. Here we report a CuO-MoS_2/MoO_3 precatalyst that undergoes electrochemical reconstruction under working conditions to yield two distinct active phases: Cu-MoS_2 for the hydrogen evolution reaction (HER) at the cathode and an optimized CuO-MoS_2/MoO_3 for the oxygen evolution reaction (OER) at the anode. In 1.0 M KOH, the reconstructed electrodes deliver remarkably low overpotentials of 35 mV for HER and 124 mV for OER at 10 mA cm^{-2}, along with outstanding long-term durability, sustaining 500 mA cm^{-2} for 100 h. Combined *in situ* Fourier-transform infrared spectroscopy and density functional theory calculations reveal that Cu species not only enhance charge transport but also tailor the electronic structure to optimize intermediate adsorption and reorganize interfacial water into a strongly hydrogen-bonded network, thereby accelerating

[1]School of Materials Science and Engineering, Hefei University of Technology, Hefei 230009, Anhui, China.
[2]Department of Materials Science and Engineering & Center of Super-Diamond and Advanced Films (COSDAF), City University of Hong Kong, Kowloon, Hong Kong 99907, China.
[3]China International S&T Cooperation Base for Advanced Energy and Environmental Materials & Anhui Provincial International S&T Cooperation Base for Advanced Energy Materials, Key Laboratory of Advanced Functional Materials and Devices of Anhui Province, Hefei University of Technology, Hefei 230009, Anhui, China.
[#]Authors contributed equally.

[*]**Correspondence to:** Dr. Yan Wang, School of Materials Science and Engineering, Hefei University of Technology, Hefei 230009, Anhui, China. E-mail: stone@hfut.edu.cn; Dr. Yucheng Wu, School of Materials Science and Engineering, Hefei University of Technology, Hefei 230009, Anhui, China; China International S&T Cooperation Base for Advanced Energy and Environmental Materials & Anhui Provincial International S&T Cooperation Base for Advanced Energy Materials, Key Laboratory of Advanced Functional Materials and Devices of

Anhui Province, Hefei University of Technology, Hefei 230009, Anhui, China. E-mail: ycwu@hfut.edu.cn; Dr. Wenjun Zhang, Department of Materials Science and Engineering & Center of Super-Diamond and Advanced Films (COSDAF), City University of Hong Kong, Kowloon, Hong Kong 99907, China. E-mail: apwjzh@cityu.edu.hk

water dissociation and proton transfer kinetics. When assembled into an anion-exchange-membrane water electrolyzer, the system delivers 1.0 A cm^{-2} at a low voltage of 1.77 V and 80 °C, with stable operation for 500 h, substantially surpassing noble-metal benchmarks. Our findings offer an efficient and durable catalyst system for sustainable hydrogen production, as well as fundamental insights into catalyst reconstruction and interfacial water regulation that inform the rational design of electrocatalytic materials.

INTRODUCTION

Mounting energy shortages and environmental degradation have driven the pursuit of green and renewable energy sources. Owing to its high gravimetric energy density, non-polluting nature, and carbon-free combustion, hydrogen is regarded as a viable substitute for fossil fuels[1,2]. Electrocatalytic water splitting, powered by renewable electricity, provides a clean and efficient route to generate high-purity hydrogen[3,4]. This process comprises two half-reactions: hydrogen evolution reaction (HER) at the cathode and oxygen evolution reaction (OER) at the anode[5,6]. While noble metals (e.g., Pt for HER and IrO_2 or RuO_2 for OER) exhibit high catalytic activity, their prohibitive cost and limited reserves hinder large-scale application[7,8]. Consequently, it is imperative to develop low-cost, earth-abundant non-precious metal electrocatalysts capable of delivering industrial-level performance for water splitting.

Molybdenum chalcogenides and oxides, particularly MoS_2 and MoO_x, have recently gained traction as viable non-precious electrocatalysts, attributable to their compositionally tunable electronic bands, affordability, and natural reserves[9,10]. Specifically, MoS_2 is celebrated for its HER-active edge terminals that afford near-optimal hydrogen chemisorption energy, albeit with largely passive basal planes[11]. In response, tactics such as defect engineering, phase modification, and heteroatom substitution have been deployed to amplify the density of active sites[12-16]. In parallel, MoO_x and its derivatives are increasingly recognized for OER, capitalizing on their flexible oxidation states to expedite redox transitions and their layered topologies to permit facile chemical intercalation[17,18]. Consequently, constructing integrated bifunctional electrodes based on MoS_2/MoO_x hetero-interfaces has emerged as a promising route to achieve efficient overall water splitting within a unified electrolyte[19,20]. Nevertheless, the suboptimal intrinsic conductivity of these molybdenum-based materials continues to curtail electron movement, posing a persistent bottleneck for their practical exploitation.

To overcome this limitation, heteroatom doping has been widely investigated, and the incorporation of copper has proven especially efficacious for MoS_2/MoO_x systems[21,22]. Cu doping dramatically upgrades the pristine electrical conductivity by fostering electron delocalization across Mo-S bonds and opening up auxiliary channels for charge flow[23-25]. More importantly, the inserted Cu species concurrently rearrange the charge density surrounding the molybdenum active sites. Such electronic perturbation serves to optimize the Gibbs free energy of pivotal reaction intermediates, such as $^*H$ for HER and $^*OOH/^*OH$ for OER, thereby reducing the energy barriers for both half-reactions[26,27]. Mechanistically, the electron-donating nature of Cu enriches the electron population at sulfur sites, which strengthens proton adsorption and eases hydrogen desorption for HER, while also promoting the necessary oxidation-state shifts and deprotonation steps for OER[28-30]. Furthermore, Cu species contribute to the reorganization of the interfacial water structure by establishing an optimized hydrogen-bonding network, which accelerates water dissociation and proton transfer at the electrode-electrolyte interface[31-33]. This structured aqueous microenvironment promotes the Volmer step in HER and facilitates nucleophilic attack and intermediate deprotonation in OER[34,35]. By

concurrently enhancing conductivity, modulating electronic structure, and engineering a kinetically friendly interfacial micro-environment, copper integration delivers a synergistic enhancement in both catalytic efficacy and longevity, charting a viable path for advancing sustainable energy conversion.

Herein, we have constructed a CuO-MoS_2/MoO_3 precatalyst via anchoring CuO nanodots onto MoS_2/MoO_3 nanosheets for electrocatalytic overall water splitting. Notably, this precursor dynamically reconstitutes under applied bias into two operationally distinct architectures, forming Cu-MoS_2 at the cathode for HER and an optimized CuO-MoS_2/MoO_3 structure at the anode for OER. The reconstructed cathode delivers a low overpotential of 35 mV at 10 mA cm^{-2} for HER, while the anode achieves an overpotential of 124 mV at the identical current density for OER. Both electrodes demonstrate exceptional operational stability, upholding a current density of 500 mA cm^{-2} for 100 h with negligible degradation. When deployed as paired electrodes in an anion-exchange-membrane water electrolyzer (AEMWE), the system requires only 1.77 V to reach 1.0 A cm^{-2} at 80 °C and retains this performance continuously for 500 h, surpassing the state-of-the-art Pt/C||RuO_2 benchmark. *In situ* Fourier-transform infrared (FTIR) and density functional theory (DFT) calculations reveal that the reconstructed Cu species not only enhance charge transport but also optimize the electronic structure of active sites, lower the energy barriers for intermediate adsorption/desorption, and reorganize interfacial water into a strongly hydrogen-bonded network, collectively boosting the overall reaction kinetics. This work provides an effective strategy for designing efficient and robust electrocatalysts toward industrial water splitting.

EXPERIMENTAL

Preparation of CuO-MoS_2/MoO_3 sample

The synthesis of CuO-MoS_2/MoO_3 samples followed a three-step protocol. Initially, commercial MoS_2 (2 g, Aladdin) and Cu powders (1 g, Sigma-Aldrich) were soaked in liquid nitrogen for 8 h. Subsequently, the cryo-treated powders were dispersed in a 200 mL mixed solvent composed of isopropyl alcohol (Sinopharm Chemical Reagent Co., Ltd.) and deionized water (v/v ratio of 1:1) via ultrasound liquid phase exfoliation conducted at 180 W for 4 h. The resulting exfoliated solution was then centrifuged at 8,000 rpm for 30 min to collect the composite of Cu nanodots and MoS_2 nanosheets. Finally, the as-obtained Cu-MoS_2 powder was transformed into the CuO-MoS_2/MoO_3 sample through annealing in air at 500 °C for 2 h.

Material characterization

Morphological features of the catalysts were examined by transmission electron microscopy (TEM, JEM-2100F) and spherical aberration correction scanning transmission electron microscopy (AC-STEM, JEM-ARM200F). X-ray diffraction (XRD) patterns were acquired on a PANalytical X-Pert PRO MPD diffractometer employing a Cu Kα source operating at 40 kV and 40 mA. X-ray photoelectron spectroscopy (XPS) measurements were performed with an ESCALAB 250Xi spectrometer. Raman spectra were recorded using a LabRAM HR Evolution spectroscopy. *In situ* FTIR spectroscopy was carried out on a Nicolet iS50 spectrometer coupled with an H-type electrochemical cell (Gaossunion Technology Co., Ltd.) to monitor the reaction intermediates.

Electrochemical measurements

All electrochemical tests were conducted on a CHI760E workstation in 1.0 M KOH alkaline electrolyte, using a standard H-type three-electrode cell with a saturated calomel electrode (SCE) as the reference electrode and a carbon rod as the counter electrode. The as-prepared CuO-MoS_2/MoO_3 sample deposited on the carbon cloth served as the working electrode. Polarization curves for both HER and OER were obtained at a scan rate of 5 mV s^{-1} with 90% *iR*-compensation. All measured potentials were converted to the reversible hydrogen electrode (RHE) scale according to the equation: $E_{RHE} = E_{SCE} + 0.059\ pH + 0.241\ V$[19]. Electrochemical impedance spectroscopy (EIS) was recorded over a frequency range of 0.01 to 10^5 Hz, with

applied potentials of -0.3 V *vs*. RHE for HER and 1.2 V *vs*. RHE for OER. The electrochemically active surface area (ECSA) was estimated from the double-layer capacitance (C_{dl}), derived from cyclic voltammetry (CV) curves at scan rates varying from 10 to 200 mV s^{-1}. The non-Faradic potential windows of 0-0.1 V *vs*. RHE and 1.0-1.1 V *vs*. RHE were selected for HER and OER, respectively. The electrocatalytic overall water splitting was evaluated on a membrane electrode assembly (MEA) configuration, employing a reconstructed Cu-MoS_2 cathode and a CuO-MoS_2/MoO_3 anode separated by an anion-exchange membrane (AEM).

DFT calculations

All DFT calculations were performed using the CP2K package with the Quickstep module[36,37]. The input file was generated using Multiwfn 3.8[38,39]. Periodic boundary conditions were imposed along the *x* and *y* directions, with a vacuum layer of 15-20 Å introduced along the *z*-axis to avoid periodic interactions. The Perdew-Burke-Ernzerhof (PBE) functional incorporating Grimme's DFT-D3 (BJ) dispersion correction was adopted within the generalized gradient approximation (GGA) to treat exchange-correlation and van der Waals forces[40,41]. Core electrons were described by norm-conserving Goedecker-Teter-Hutter (GTH) pseudopotentials, while valence electrons were expanded with the DZVP-MOLOPT-SR-GTH basis set[42]. A plane-wave cutoff of 400 Ry and a relative cutoff of 55 Ry were set. The DFT + U method was applied to Mo atoms to better capture the localized d-electron behavior. Geometry optimization was performed using the Broyden-Fletcher-Goldfarb-Shanno (BFGS) algorithm, with convergence criteria of 4.5×10^{-4} Ha/Bohr for maximum force and 3.0×10^{-3} Bohr for maximum displacement. During optimization, the bottom two atomic layers were kept fixed to simulate surface constraints. SCF convergence was accelerated by the direct inversion in the iterative subspace (DIIS) minimizer and a full preconditioner, with an energy tolerance of 1.0×10^{-5}.

RESULTS AND DISCUSSION

Characterizations of CuO-MoS_2/MoO_3 nanosheets

The CuO-MoS_2/MoO_3 nanosheets were obtained via controlled oxidation of the exfoliated Cu-MoS_2 precursor. XRD analysis [Figure 1A] verified the coexistence of diffraction peaks ascribed to MoO_3, MoS_2, and CuO phases, confirming the successful formation of a ternary composite. This assignment was further substantiated by Raman spectroscopy [Figure 1B], which distinctly captured the characteristic vibrational signatures of all three constituents, offering complementary structural confirmation. Transmission electron microscopy [Figure 1C] disclosed typical nanosheet morphologies decorated with CuO nanodots that were evenly spread over the MoS_2/MoO_3 support. This homogeneous distribution was more clearly visualized in spherical aberration-corrected STEM images [Figure 1D], where the embedded CuO nanodots appeared as bright spots exhibiting strong contrast against the underlying substrate. High-resolution TEM analysis [Figure 1E] resolved clear lattice fringes with measured spacings of 0.270, 0.232, and 0.227 nm, indexed respectively to the (101) plane of MoO_3, the (111) plane of CuO, and the (103) plane of MoS_2. The presence of these three distinct spacings within the same region attests to the intimate interfacial contact among the different phases. Additionally, elemental mapping [Figure 1F] confirmed the uniform spatial distribution of O, Cu, Mo, and S throughout the composite architecture, indicating that CuO nanodots were well incorporated into the MoS_2/MoO_3 matrix and that a thoroughly mixed ternary material had been formed.

XPS analysis was conducted to probe the surface chemical states of CuO-MoS_2/MoO_3 in parallel with MoS_2/MoO_3 for reference. The Cu 2p spectrum [Figure 1G] exhibited distinct peaks at 934.5 eV for Cu $2p_{3/2}$ and 954.6 eV for Cu $2p_{1/2}$, accompanied by pronounced shake-up satellite features, which are characteristic of Cu^{2+} oxidation state[43]. The high-resolution Mo 3d spectrum of CuO-MoS_2/MoO_3 [Figure 1H] displayed two characteristic peaks at 233.3 and 236.4 eV, corresponding to Mo^{4+} and Mo^{6+}, respectively[19,44]. A notable positive shift in binding energy was observed for these Mo 3d peaks compared to those in MoS_2/MoO_3 (232.9 and 236.0 eV, Supplementary Figure 1), suggesting a modified electronic environment around Mo centers

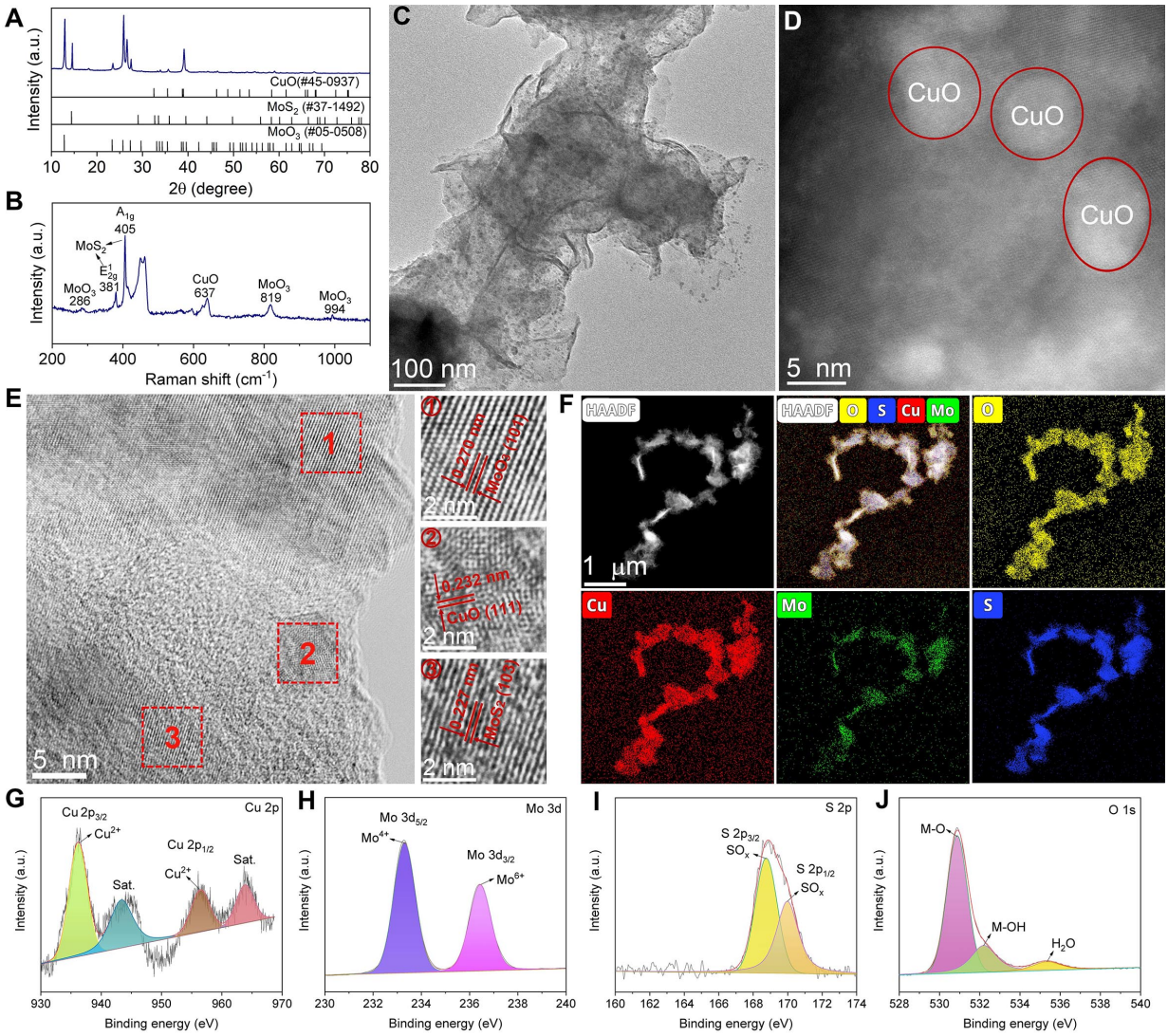

Figure 1. Characterizations of precatalysts. (A) XRD pattern; (B) Raman spectrum; (C) TEM image; (D) AC-STEM image; (E) HR-TEM image; (F) Elemental mapping of CuO-MoS_2/MoO_3 nanosheets; XPS spectra of (G) Cu 2p, (H) Mo 3d, (I) S 2p, and (J) O 1s for CuO-MoS_2/MoO_3 nanosheets.

due to electron transfer toward CuO species. In the S 2p region [Figure 1I], the doublet located at 168.7 eV for S $2p_{3/2}$ and 169.9 eV for S $2p_{1/2}$ further confirmed the presence of SO_x species in the MoS_2/MoO_3 phase[20]. Moreover, the O 1s spectrum [Figure 1J] was well-fitted with three components, including lattice oxygen in metal oxides (Mo) at 530.9 eV, surface hydroxyl groups (M-OH) at 532.2 eV, and adsorbed water molecules at 535.4 eV[45]. Collectively, these results confirm the successful synthesis of CuO-MoS_2/MoO_3 precatalyst.

Identification of the actual catalytic species

The as-prepared CuO-MoS_2/MoO_3 precatalyst was subjected to appreciable electrochemical reconstruction during electrolytic operation. To track this transformation and clarify the true active species under working conditions, we performed *in situ* electrochemical XRD to monitor phase evolution in real time for both HER and OER, given the composition dynamics induced by applied potentials. For the HER process [Figure 2A and B], the CuO-MoS_2/MoO_3 precatalyst initially showed coexisting phases of CuO, MoO_3, and MoS_2 at open circuit potential (OCP). Upon applying a cathodic potential of -0.1 V *vs.* RHE, the CuO and MoO_3 peaks gradually diminished, while metallic Cu phases emerged and intensified with increasing

cathodic polarization. Quantitative analysis revealed that the CuO (111) peak at 2θ = 35.5° decreased by 92% and became undetectable at -0.3 V *vs.* RHE, confirming complete reduction to metallic Cu, with new peaks emerging at 2θ = 43.3°, 50.4°, and 74.1° corresponding to the (111), (200), and (220) planes of Cu (JCPDS No. 04-0836). Similarly, the MoO_3 (101) peak intensity diminished by 87% and became undetectable at -0.3 V *vs.* RHE. In contrast, the MoS_2 phase maintained its structural integrity throughout the HER process without detectable formation of other Mo-containing species. These findings point to the electrochemical reduction of CuO to metallic Cu coupled with preservation of MoS_2, suggesting that the reconstructed Cu-MoS_2 constitutes the genuine HER-active phase. Turning to the OER side [Figure 2C and D], the catalyst exhibited distinct reconstruction behavior. The CuO and MoS_2 phases remained stable across the potential range from OCP to 1.50 V *vs.* RHE, while the MoO_3 phase underwent partial reconstruction at 1.10-1.15 V *vs.* RHE, as evidenced by reduced diffraction peak intensity. Notably, the MoO_3 (101) peak shows a maximum intensity decrease of only 38% at 1.15 V *vs.* RHE, which subsequently recovers to 85% of its original intensity at 1.50 V *vs.* RHE, confirming partial and reversible reconstruction. The CuO (111) peak maintains 95% of its original intensity throughout the OER potential range, indicating structural stability under anodic conditions. These quantitative differences substantiate the complete reconstruction of CuO-MoS_2/MoO_3 into Cu-MoS_2 for HER, while maintaining an optimized CuO-MoS_2/MoO_3 structure for OER.

Post-reaction AC-STEM characterization [Figure 2E and F] provided deeper structural insights into the reconstructed catalysts. After HER testing, finely dispersed Cu clusters were distinctly observed on the MoS_2 (103) plane, corroborating the formation of Cu-MoS_2. Following OER testing, distinct lattice spacings of 0.227 and 0.270 nm were observed, corresponding to the (103) plane of MoS_2 and (101) plane of MoO_3, respectively, with CuO clusters embedded in the MoS_2/MoO_3 matrix. Notably, both Cu and CuO clusters in the reconstructed catalysts exhibited significantly reduced sizes compared to the original CuO nanodots, indicating that electrochemical reconstruction generates finer, highly dispersed active species with potentially enhanced catalytic properties. XPS measurements were conducted to analyze the surface chemical states of the reconstructed catalysts [Figure 2G-J]. The reconstructed CuO-MoS_2/MoO_3 after OER still showed characteristic peaks of Cu^{2+} species, whereas Cu-MoS_2 gave distinct signals attributable to Cu^0 or Cu^+ species, confirming the reduction of pristine CuO during HER operation. The appearance of Cu^{2+} species in the air-exposed Cu-MoS_2 sample was attributed to surface reoxidation. Similar surface oxidation phenomena were observed for Mo and S elements in Cu-MoS_2, manifested as Mo^{6+} and SO_x species[46,47]. By contrast, the reconstructed CuO-MoS_2/MoO_3 catalyst showed enhanced peak intensities for Mo^{6+} and SO_x species, together with the emergence of metal-oxygen (M-O) bonds in the O 1s spectrum, collectively demonstrating the coexistence of MoS_2 and MoO_3 phases in this OER-active material[47]. This comprehensive characterization provides compelling evidence that the electrochemical reconstruction process generates distinct, optimized active structures for HER and OER, with the transformed interfacial chemistry playing a crucial role in enhancing catalytic performance.

Evaluation of electrocatalytic HER and OER performance

The HER activity of the reconstructed Cu-MoS_2 electrode was assessed in a 1.0 M KOH within a standard three-electrode cell. For comparison, pure Cu, MoS_2, and commercial 20% Pt/C electrodes were also measured under identical conditions. As revealed by the polarization curves in Figure 3A, the Cu-MoS_2 electrode exhibited a sharp increase in cathodic current with increasing overpotential, demonstrating significantly enhanced HER activity compared to the reference materials. Quantitative analysis of the polarization data [Figure 3B] shows that the Cu-MoS_2 electrode required remarkably low overpotentials of only 35, 54, 112, and 287 mV to deliver current densities of 10, 50, 100, and 500 mA cm^{-2}, respectively. These values are substantially lower than those required by pure Cu, MoS_2, and even the Pt/C benchmark, particularly at higher current densities relevant to industrial applications. Further investigation of the HER kinetics through Tafel slope analysis, which was obtained from the linear regions of the Tafel plots with 90%

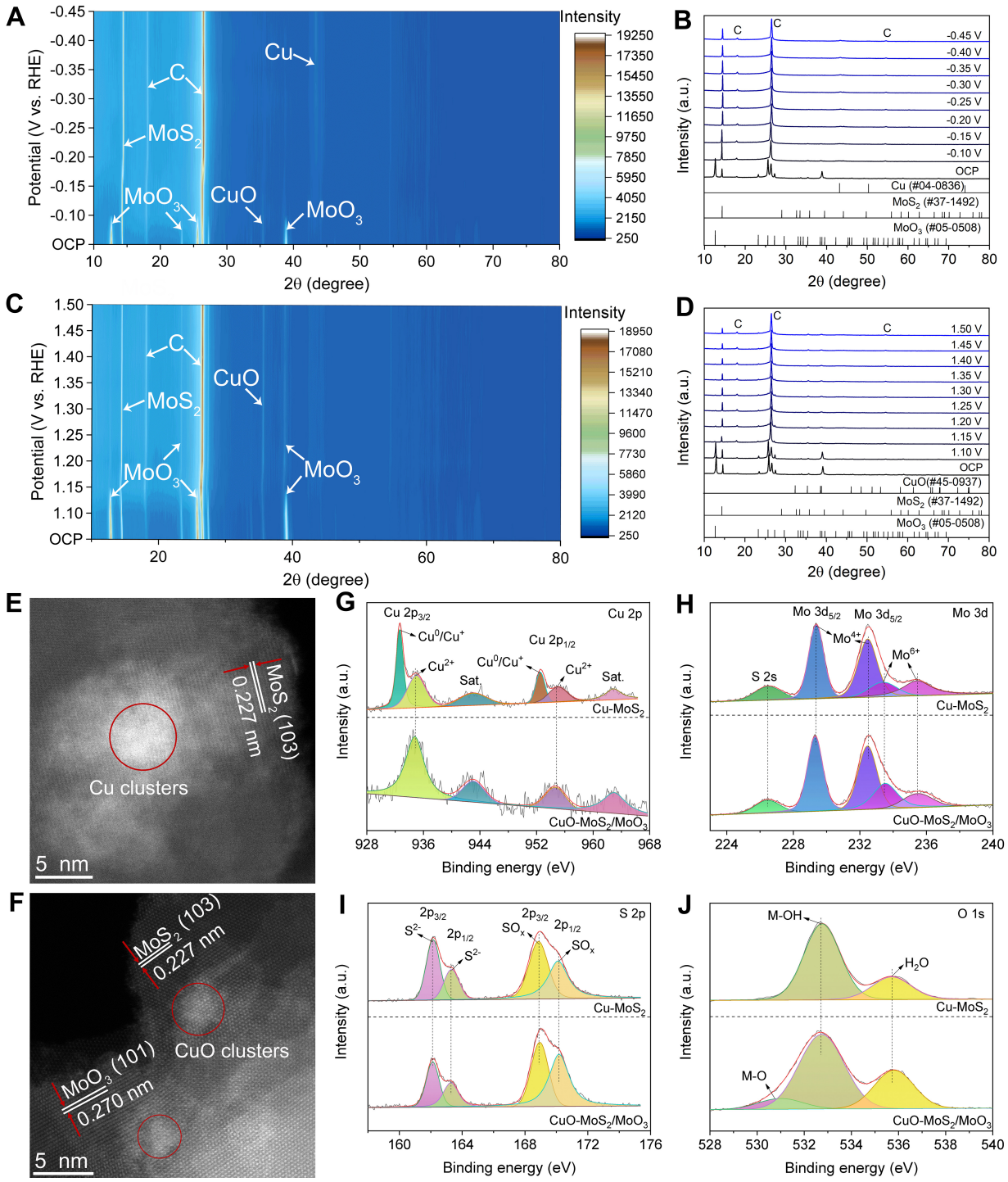

Figure 2. Characterizations of the reconstructed catalysts. (A and B) *In situ* XRD patterns of CuO-MoS_2/MoO_3 during HER process; (C and D) *In situ* XRD patterns of CuO-MoS_2/MoO_3 during OER process; AC-STEM images of (E) Cu-MoS_2 and (F) CuO-MoS_2/MoO_3 after reaction; XPS spectra of (G) Cu 2p, (H) Mo 3d, (I) S 2p, and (J) O 1s in Cu-MoS_2 and CuO-MoS_2/MoO_3.

iR compensation. As shown in Figure 3C, the Cu-MoS_2 electrode displayed a favorable slope of 168.9 mV dec^{-1}, significantly smaller than those of Cu (252.7 mV dec^{-1}) and MoS_2 (191.6 mV dec^{-1}). These values, while higher than those typically reported in acidic media, were consistent with alkaline water

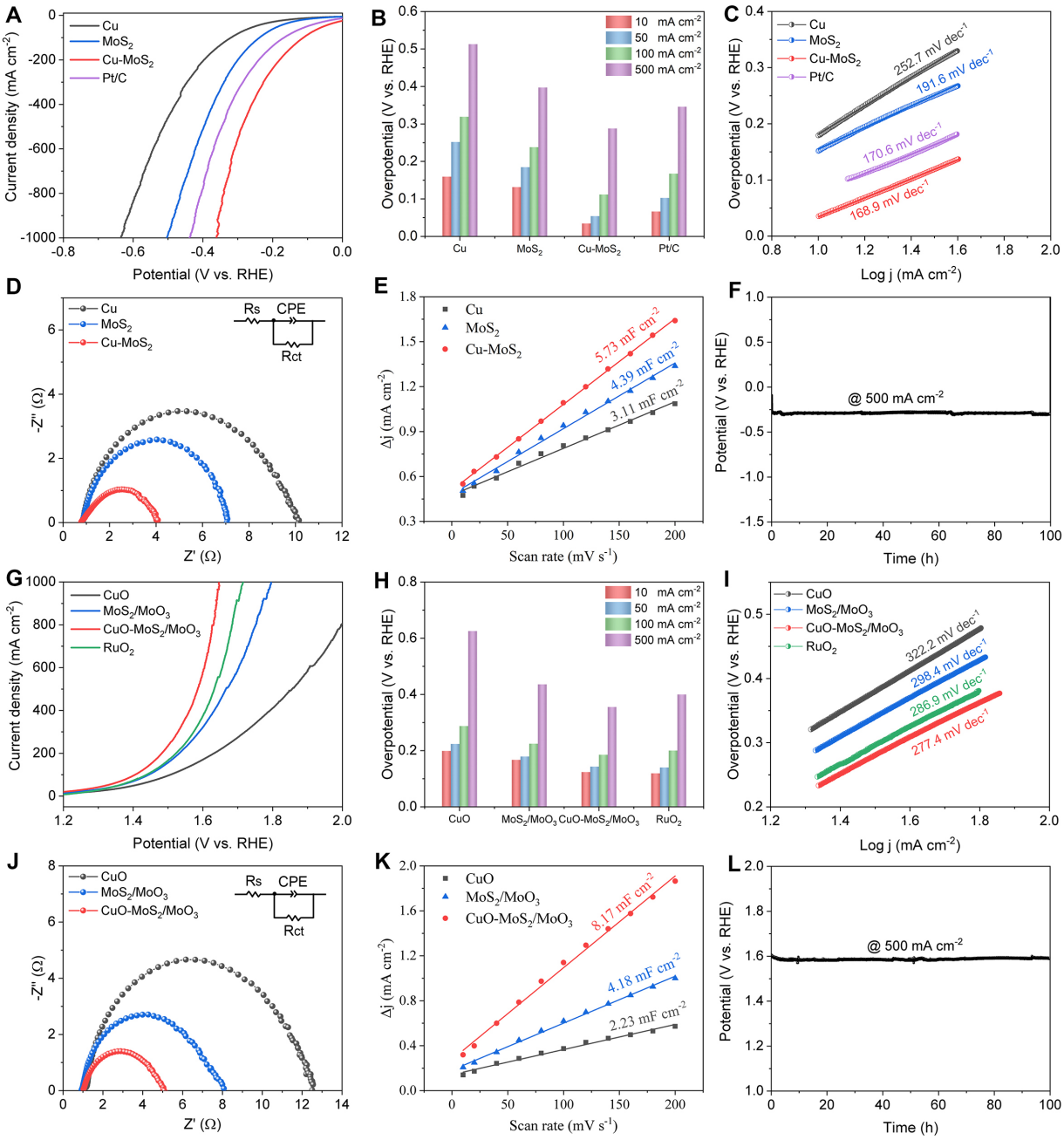

Figure 3. Electrochemical performance of HER and OER. (A) LSV curves; (B) Overpotentials; (C) Tafel plots; (D) EIS spectra; (E) C_{dl} values of Cu-MoS_2 and control catalysts for HER; (F) Chronopotentiometric curve of Cu-MoS_2 at 500 mA cm^{-2} for 100 h; (G) LSV curves; (H) Overpotentials; (I) Tafel plots; (J) EIS spectra; (K) C_{dl} values of CuO-MoS_2/MoO_3 and control catalysts for OER; (L) Chronopotentiometric curve of CuO-MoS_2/MoO_3 at 500 mA cm^{-2} for 100 h.

splitting, where the Volmer step (water dissociation) introduced an additional kinetic barrier. For comparison, commercial Pt/C in 1.0 M KOH exhibited a Tafel slope of 170.6 mV dec^{-1} under identical conditions, confirming that the measured values were reasonable for alkaline electrolytes. The HER Tafel slope suggested a Volmer-Heyrovsky mechanism with the electrochemical adsorption step being rate-limiting[48].

EIS measurements were employed to probe the interfacial charge transfer kinetics. The Nyquist plots [Figure 3D] show that the Cu-MoS_2 electrode exhibited the smallest charge-transfer resistance (R_{ct} = 3.2 Ω) among all samples, signifying markedly accelerated electron transfer during the HER process. To evaluate the

ECSA, C_{dl} was determined from CV scans in the non-Faradaic potential region [Supplementary Figure 2]. The Cu-MoS_2 electrode displayed the highest C_{dl} value of 5.73 mF cm^{-2} [Figure 3E], confirming a substantial increase in the number of accessible active sites compared to the reference materials. To evaluate the intrinsic activity, we normalized the catalytic current by the ECSA using the measured C_{dl} values [Supplementary Figure 3]. At an overpotential of 100 mV, the ECSA-normalized HER current density for Cu-MoS_2 reached 0.611 mA cm^{-2}_{ECSA}, which is 3.94 and 3.99 times higher than those of MoS_2 (0.155 mA cm^{-2}_{ECSA}) and Cu (0.153 mA cm^{-2}_{ECSA}), respectively. The corresponding turnover frequency (TOF) at the same overpotential, calculated based on the ECSA-derived active site density (assuming 10^{15} sites cm^{-2}, i.e., 1.66×10^{-9} mol cm^{-2}), was 1.91 s^{-1} for Cu-MoS_2 [Supplementary Table 1], significantly exceeding that of MoS_2 (0.48 s^{-1}) and Cu (0.48 s^{-1}). The mass activity of Cu-MoS_2 reached 175.2 A g^{-1} at 100 mV, substantially higher than MoS_2 (34.0 A g^{-1}) and Cu (23.8 A g^{-1}). These results demonstrate that the enhanced catalytic performance originates from improved intrinsic activity of the active sites, not merely from increased surface area. Moreover, the Cu-MoS_2 catalyst demonstrated outstanding operational stability, maintaining a constant current density of 500 mA cm^{-2} for 100 h without apparent potential decay [Figure 3F]. This exceptional stability, combined with superior activity and favorable kinetics, positions the Cu-MoS_2 electrode as a highly promising catalyst for practical hydrogen production applications.

The OER performance of the CuO-MoS_2/MoO_3 electrode was rigorously evaluated in 1.0 M KOH electrolyte using a standard three-electrode system. As clearly depicted in the polarization curves [Figure 3G], the CuO-MoS_2/MoO_3 electrode demonstrated a substantially steeper increase in anodic current density with applied potential compared to all control electrodes, including CuO, MoS_2/MoO_3, and RuO_2. This pronounced activity enhancement is quantitatively reflected in the exceptionally low overpotentials needed to attain 10, 50, 100, and 500 mA cm^{-2}, which were measured at only 124, 143, 185, and 355 mV, respectively [Figure 3H]. These values represent significant improvements over the corresponding overpotentials of the reference catalysts, particularly at higher current densities relevant to industrial applications.

Further insight into the OER kinetics was obtained through Tafel analysis [Figure 3I]. The CuO-MoS_2/MoO_3 electrode exhibited a Tafel slope of 277.4 mV dec^{-1}, which is notably lower than those of MoS_2/MoO_3 (298.4 mV dec^{-1}), CuO (322.2 mV dec^{-1}), and RuO_2 (286.9 mV dec^{-1}). The OER Tafel slope likely reflected surface coverage effects or a chemical rate-determining step (RDS), yet the CuO-MoS_2/MoO_3 catalyst still exhibited the lowest Tafel slope among all tested samples, demonstrating superior reaction kinetics[49]. EIS measurements provided additional evidence for enhanced reaction kinetics, showing the smallest charge-transfer resistance (R_{ct} = 4.0 Ω) for CuO-MoS_2/MoO_3 among all samples [Figure 3J], suggesting significantly facilitated charge transfer during the OER process[50]. In addition, the CuO-MoS_2/MoO_3 electrode displayed the highest C_{dl} value of 8.17 mF cm^{-2} [Figure 3K and Supplementary Figure 4], substantially larger than those of the counterpart materials, indicating a greater number of accessible active sites contributing to the improved OER activity[51]. At an overpotential of 200 mV, the CuO-MoS_2/MoO_3 catalyst exhibited an ECSA-normalized current density of 0.612 mA cm^{-2}_{ECSA} with a TOF of 0.956 s^{-1} and a mass activity of 250.0 A g^{-1} [Supplementary Figure 5 and Supplementary Table 2]. At 500 mV, the corresponding values increased to 5.981 mA cm^{-2}_{ECSA}, 9.33 s^{-1}, and 2,442.8 A g^{-1}, respectively. The mass activity of CuO-MoS_2/MoO_3 at 500 mV is 1.74 times higher than that of MoS_2/MoO_3 (1,406.8 A g^{-1}) and 3.92 times higher than CuO (623.7 A g^{-1}). It is noteworthy that the promotional effect of Cu species exhibits distinct characteristics for HER and OER: for HER, Cu incorporation significantly enhances the intrinsic activity per active site, while for OER, CuO decoration primarily increases the number of accessible active sites. These distinct yet complementary mechanisms collectively demonstrate the versatility of Cu/CuO modification in tailoring catalytic properties for different half-reactions. These results unequivocally demonstrate that the enhanced catalytic performance originates from improved intrinsic activity of the active sites, not merely from increased surface area, confirming the critical role of Cu incorporation in promoting the electrocatalytic activity of the Mo-based

catalyst system. Moreover, the catalyst demonstrated exceptional operational stability, maintaining nearly constant performance over 100 h of continuous operation at 500 mA cm^{-2} with negligible activity loss [Figure 3L]. These results indicate that the incorporation of CuO nanodots into MoS_2/MoO_3 nanosheets markedly enhances both HER and OER performance. This improvement can be attributed to the formation of highly active Cu-Mo interfacial sites, which synergistically promote water dissociation, facilitate charge transfer kinetics, and increase the density of ECSAs, positioning this material as a promising alternative to noble metal-based catalysts for practical water splitting applications.

Mechanism investigations

To probe deeper into the water splitting mechanism, we employed *in situ* FTIR spectroscopy to examine the behavior of interfacial water molecules on Cu-MoS_2 and CuO-MoS_2/MoO_3 surfaces. The *in situ* FTIR spectra [Figure 4A and B, and Supplementary Figure 6] revealed two characteristic vibrational modes of adsorbed water molecules at 1,640 and 2,800~3,700 cm^{-1}, corresponding to the H-O-H bending and O-H stretching band, respectively[52,53]. Notably, both vibrational bands exhibited significantly enhanced intensity on Cu-MoS_2 during HER compared to MoS_2 [Supplementary Figure 7], demonstrating substantially improved water adsorption capability resulting from Cu incorporation. A parallel enhancement was observed for CuO-MoS_2/MoO_3 relative to MoS_2/MoO_3 under OER conditions [Supplementary Figure 8]. Time-dependent *in situ* FTIR measurements [Supplementary Figure 9] further captured the progressive accumulation of water-related signals during electrolysis, confirming continuous and efficient water activation on the catalyst surfaces throughout the electrochemical processes.

For a deeper understanding of the interfacial water structure, we performed detailed Gaussian fitting analysis of the O-H stretching region using a multi-peak fitting routine. The fitting was conducted with peak positions allowed to vary within ±10 cm^{-1} of the literature values, while the full width at half maximum (FWHM) was constrained to 150-250 cm^{-1} and a linear baseline correction was applied. All fits achieved R^2 values exceeding 0.99, confirming the high reliability of the deconvolution. This procedure resolved three distinct components centered at approximately 3,230, 3,420, and 3,550 cm^{-1} [Figure 4C and D, Supplementary Figure 10], which were assigned to symmetric strongly hydrogen-bonded water, asymmetric hydrogen-bonded water, and weakly hydrogen-bonded (isolated) water, respectively[54,55]. Peak area ratios were calculated from integrated areas after normalization to the total O-H stretching intensity. Quantitative analysis revealed a remarkable increase in the proportion of symmetric strongly hydrogen-bonded water on both Cu-MoS_2 and CuO-MoS_2/MoO_3 compared with their unmodified counterparts [Figure 4E and F]. This specific water configuration is of particular significance, as it facilitates efficient proton transfer via a well-structured hydrogen-bonding network, indicating that Cu-modified surfaces actively promote the organization of interfacial water into a more ordered and strongly bonded structure[56].

Further potential-dependent measurements provided additional mechanistic clues. The O-H stretching frequency of symmetric hydrogen-bonded water displayed a pronounced potential-dependent shift characteristic of the Stark effect [Figure 4G]. The calculated Stark slopes for Cu-MoS_2 (44.5 cm^{-1} V^{-1}) and CuO-MoS_2/MoO_3 (51.2 cm^{-1} V^{-1}) were substantially higher than those for MoS_2 (11.8 cm^{-1} V^{-1}) and MoS_2/MoO_3 (15.9 cm^{-1} V^{-1}). These markedly higher Stark slopes imply that interfacial water molecules on Cu-modified catalysts possess greater flexibility and enhanced sensitivity to applied potential, resulting in more pronounced vibrational frequency shifts under electrochemical conditions[57]. Taken together, these findings offer strong evidence that both Cu-MoS_2 and CuO-MoS_2/MoO_3 catalysts effectively promote the formation of strongly hydrogen-bonded water networks at the electrode-electrolyte interface. These structured water networks serve as efficient proton transfer pathways, thereby accelerating water dissociation

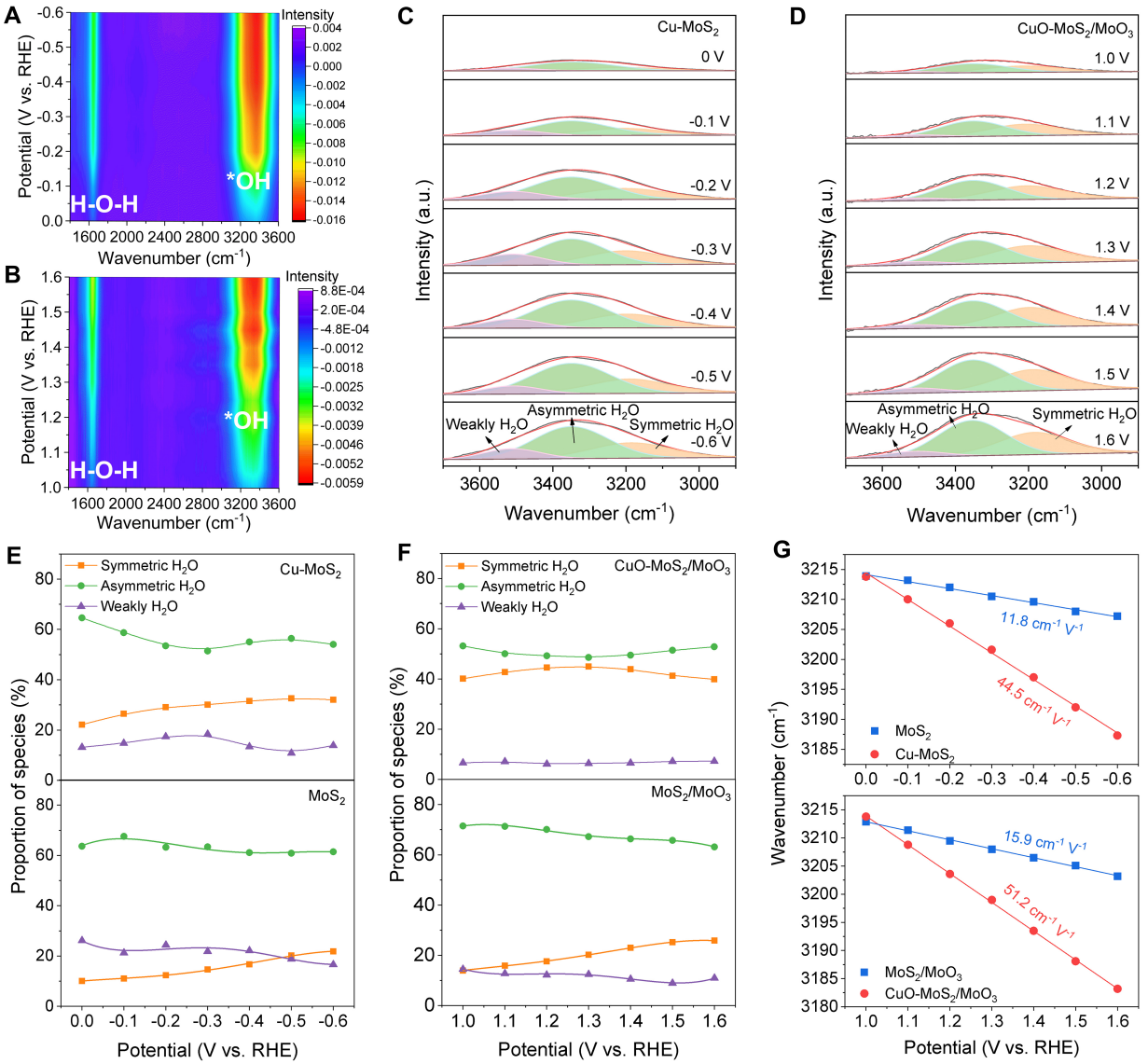

Figure 4. Identification of the interfacial water structure. *In situ* FTIR spectra of (A) Cu-MoS_2 under applied potentials from 0 to -0.6 V *vs.* RHE and (B) CuO-MoS_2/MoO_3 under applied potentials from 1.0 to 1.6 V *vs.* RHE; The Gaussian fits of three O-H stretching modes on (C) Cu-MoS_2 and (D) CuO-MoS_2/MoO_3; Potential-dependent population of the three water species on (E) Cu-MoS_2 and MoS_2 and (F) CuO-MoS_2/MoO_3 and MoS_2/MoO_3; (G) The corresponding wavenumber shift of symmetric H_2O over Cu-MoS_2 and MoS_2, and CuO-MoS_2/MoO_3 and MoS_2/MoO_3.

and proton/hydroxide transport processes, which fundamentally enhance the kinetics of both HER and OER.

DFT calculations were systematically performed to obtain atomic-level insights into the catalytic mechanisms of both HER and OER. Well-optimized structural models were constructed to represent the catalytic systems, with MoS_2 and Cu-MoS_2 serving as HER catalysts, while MoS_2/MoO_3 and CuO-MoS_2/MoO_3 models were developed for OER investigations [Supplementary Figure 11]. Differential charge density analysis [Figure 5A] revealed substantial electron redistribution at the heterointerfaces, demonstrating distinct charge transfer patterns. Specifically, Cu-MoS_2 exhibited significant electron transfer from Cu clusters to the MoS_2 substrate with a total charge transfer of 0.36 e^-, creating an electron-rich MoS_2 surface. In contrast, CuO-MoS_2/MoO_3 showed reverse electron transfer from the MoS_2/MoO_3 substrate to CuO clusters, amounting to 0.15 e^-. This pronounced interfacial charge redistribution effectively modulates the d-band centers of the catalytic sites, consequently optimizing their adsorption properties toward reaction

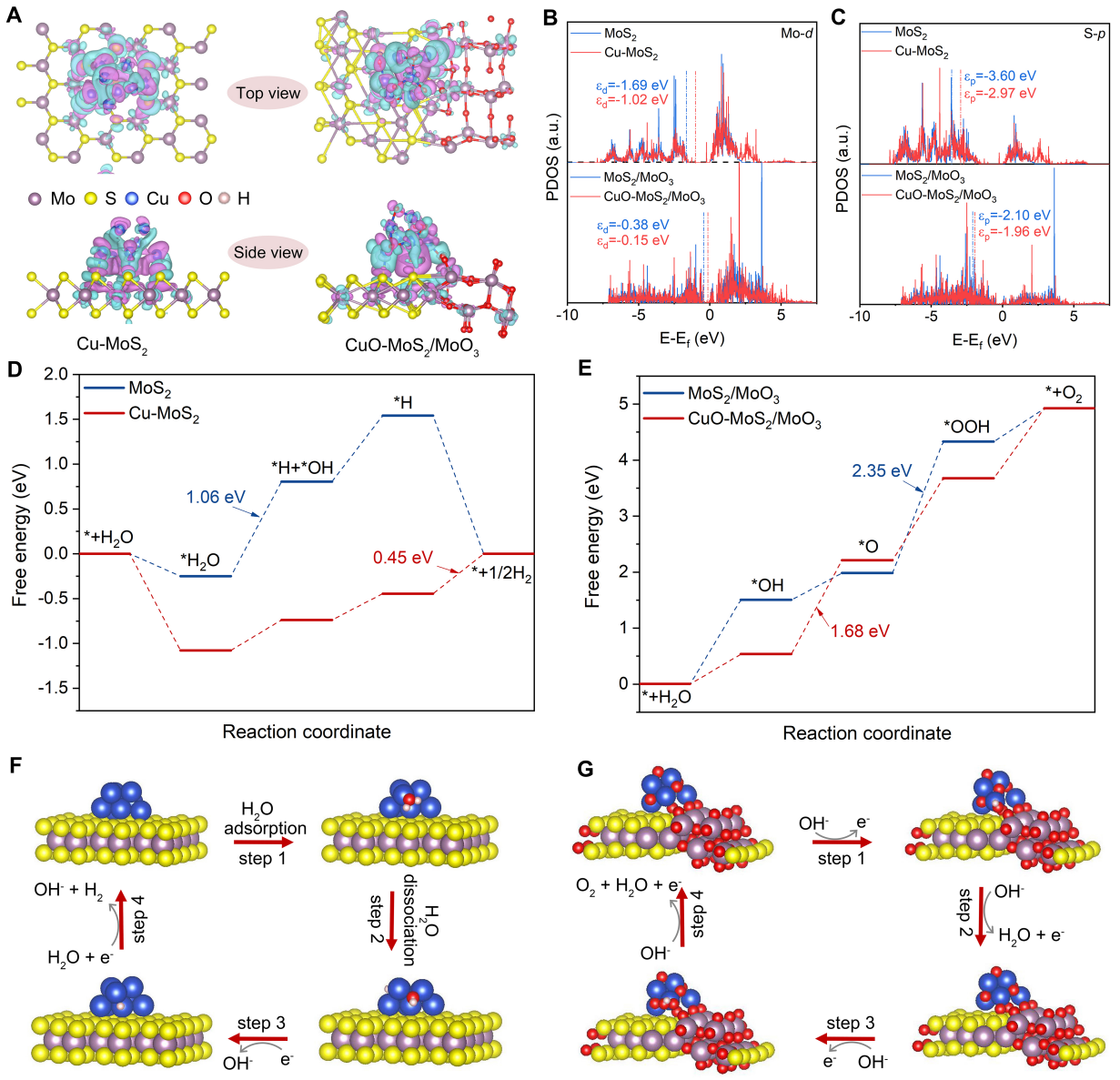

Figure 5. Theoretical investigation. (A) Differential charge density of Cu-MoS_2 and CuO-MoS_2/MoO_3 model, purple and blue regions respectively, manifests the charge accumulation and depletion; The PDOS of (B) Mo-d and (C) S-p in the four catalyst models; Gibbs free energy diagram for (D) HER process on MoS_2 and Cu-MoS_2 (Cu-Mo interfacial site), and (E) OER process on MoS_2/MoO_3 and CuO-MoS_2/MoO_3 (CuO-MoS_2/MoO_3 interfacial site); Reaction pathways of (F) HER process on Cu-MoS_2 at Cu-Mo interfacial site and (G) OER process on CuO-MoS_2/MoO_3 at CuO-MoS_2/MoO_3 interfacial site.

intermediates[58]. The partial density of states (PDOS) analysis provided further evidence of electronic structure modulation[59]. As illustrated in Figure 5B, the d-band center of Mo 3d orbitals exhibited a notable upward shift from -1.69 eV in MoS_2 to -1.02 eV in Cu-MoS_2, and similarly from -0.38 eV in MoS_2/MoO_3 to -0.15 eV in CuO-MoS_2/MoO_3. A parallel electronic modulation was observed for S 2p orbitals [Figure 5C], confirming that the incorporation of Cu/CuO clusters effectively tunes the electronic structure of both Mo and S sites, thereby enhancing the water adsorption capability and optimizing the binding strength of reaction intermediates.

The reaction energetics were quantitatively evaluated through Gibbs free energy calculations [Figure 5D and E], with detailed reaction pathways schematically illustrated in Figure 5F and G, Supplementary Figures 12 and 13. For HER on Cu-MoS_2, the RDS shifted from water dissociation on pristine

MoS_2 (1.06 eV) to hydrogen desorption on Cu-MoS_2. For Cu clusters alone, the hydrogen desorption barrier was 0.71 eV [Supplementary Figure 14]; notably, when considering the Cu-Mo interfacial site as the true catalytic center, this barrier was further reduced to only 0.45 eV, confirming that the interface between Cu and MoS_2 serves as the most active site for HER. In the case of OER, the RDS energy barrier was dramatically decreased from 2.35 eV for the *O → *OOH transformation on MoS_2/MoO_3 to 1.85 eV for the *OH → *O conversion on CuO clusters. More importantly, at the CuO-MoS_2/MoO_3 interfacial site, the RDS barrier was further lowered to 1.68 eV, demonstrating that the interfacial sites, rather than individual CuO clusters, are the genuine catalytic centers responsible for the enhanced OER performance[60,61]. These computational results clearly demonstrate that Cu incorporation, particularly at the Cu-Mo and CuO-MoS_2/MoO_3 interfaces, effectively optimizes the reaction pathways and reduces the energy barriers for both HER and OER. Integrating these computational findings with *in situ* FTIR spectroscopic results, we establish a comprehensive mechanism where both Cu-MoS_2 and CuO-MoS_2/MoO_3 catalysts synergistically optimize the adsorption/desorption behavior of key reaction intermediates while facilitating the formation of a strongly hydrogen-bonded water network at the electrode-electrolyte interface.

Electrochemical performance of overall water splitting

For a thorough assessment of the practical viability of our catalysts in industrial water electrolysis, we assembled an AEMWE featuring the reconstructed Cu-MoS_2 as the cathode and CuO-MoS_2/MoO_3 as the anode. As a benchmark, a reference cell was constructed using commercial Pt/C (20 wt% Pt) and RuO_2 as the cathode and anode, respectively, representing the state-of-the-art noble metal-based configuration. Schematic and photographic views of the AEMWE setup are presented in Figure 6A and B. Initial performance evaluation through polarization curves measured at 25 °C [Figure 6C] revealed the exceptional efficiency of our catalyst system. The Cu-MoS_2||CuO-MoS_2/MoO_3 electrolyzer required only 1.82 and 1.98 V to achieve current densities of 0.5 and 1.0 A cm^{-2}, respectively, significantly outperforming the Pt/C||RuO_2 benchmark system, which required 1.91 and 2.06 V for the same current densities. This performance advantage became even more pronounced when the operating temperature was elevated to 80 °C [Figure 6D], where the voltage required to maintain 1.0 A cm^{-2} decreased substantially from 1.98 to 1.77 V, demonstrating the system's excellent temperature responsiveness and potential for high-efficiency operation under practical industrial conditions.

The long-term stability test was performed at 1.0 A cm^{-2} and 80 °C using a closed-loop circulation system with 1.0 M KOH electrolyte circulated at 100 mL min^{-1} through both compartments. The electrolyte reservoir volume was 500 mL and was not replenished during the 500-h test. Impressively, the Cu-MoS_2||CuO-MoS_2/MoO_3 electrolyzer exhibited remarkable durability throughout the 500-h testing period [Figure 6E], maintaining stable voltage output with a minimal degradation rate of merely 23.62 μV h^{-1}. This performance stands in stark contrast to the commercial Pt/C||RuO_2 benchmark system, which suffered rapid performance degradation with a voltage increase rate of 1.03 mV h^{-1} within just 160 h of operation, representing a degradation rate approximately 44 times faster than our system. To further validate the practical applicability, we evaluated the hydrogen production power consumption and energy conversion efficiency without iR compensation. The Cu-MoS_2||CuO-MoS_2/MoO_3 electrolyzer achieved outstanding power consumption values of only 3.70 and 4.23 kWh Nm^{-3} at 0.5 and 1.0 A cm^{-2}, respectively, corresponding to remarkable energy conversion efficiencies of 79.35% and 69.49%. These efficiency metrics, combined with the comprehensive performance comparison summarized in Figure 6F and Supplementary Table 3, demonstrate that our electrolyzer surpasses previously reported AEMWE systems. These outstanding results unequivocally highlight the strong potential of our catalyst system for practical implementation in industrial-level water electrolysis applications, positioning it as a viable and efficient alternative to conventional noble metal-based technologies.

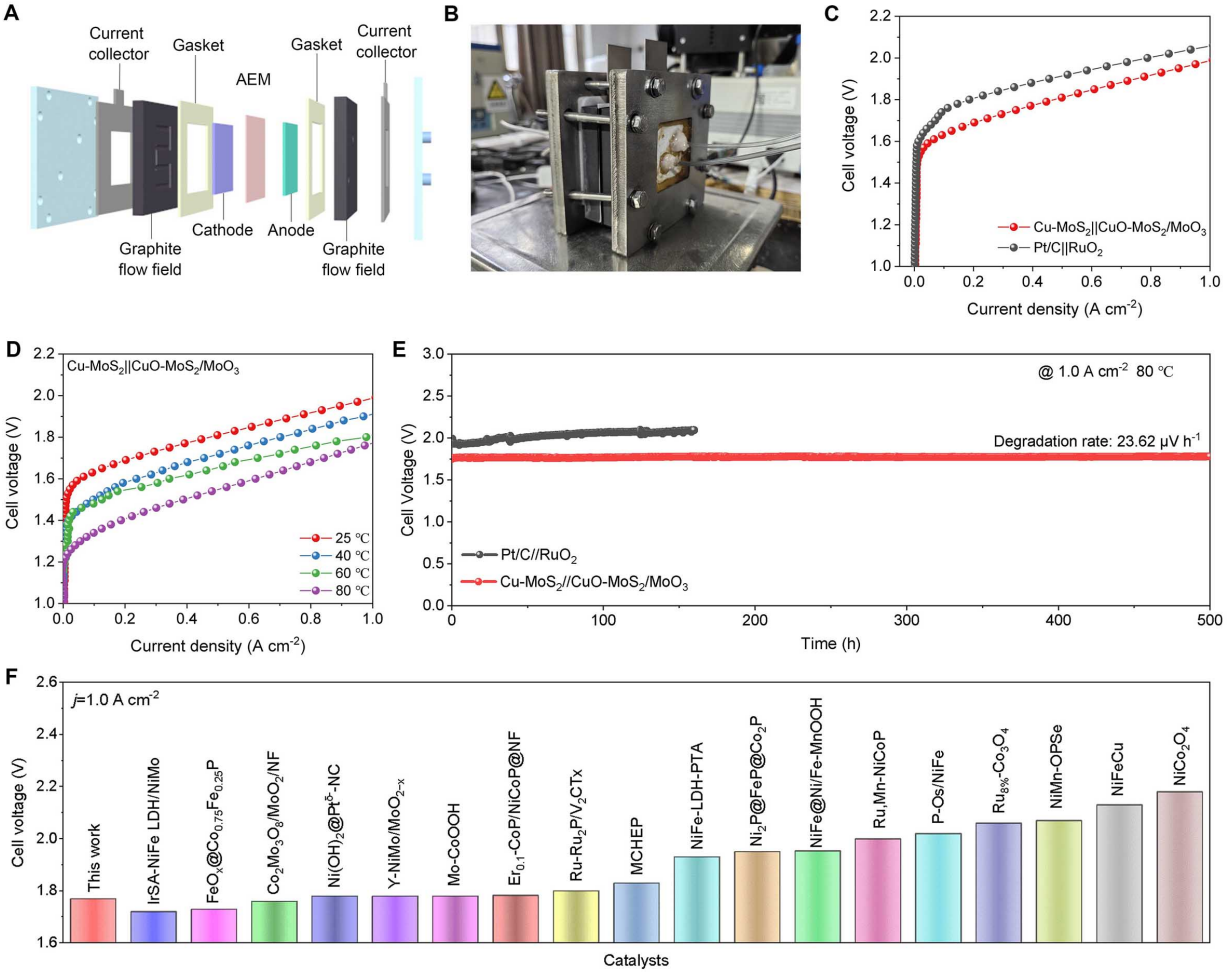

Figure 6. Performance of AEMWE for overall water splitting. (A) Schematic diagram and (B) digital photograph of the AEMWE setup, photograph taken by the authors; (C) Polarization curves of Cu-MoS_2||CuO-MoS_2/MoO_3 and Pt/C||RuO_2 electrolyzer at 25 °C; (D) Polarization curves of Cu-MoS_2||CuO-MoS_2/MoO_3 electrolyzer at different temperatures; (E) Chronopotentiometric curves of the AEMWE operated under 1.0 A cm^{-2} at 80 °C; (F) Comparison of cell voltages for the Cu-MoS_2||CuO-MoS_2/MoO_3 electrolyzer and recently reported AEM catalysts at 1.0 A cm^{-2}.

CONCLUSION

In summary, we have demonstrated the electrochemical reconstruction of the CuO-MoS_2/MoO_3 precatalyst during electrochemical water splitting. Under operating conditions, the precatalyst transforms into Cu-MoS_2 for HER while retaining an optimized structure for OER, yielding exceptional performance characterized by low overpotentials and outstanding durability at industrial current densities. Mechanistic investigations reveal that the incorporated Cu species not only optimize the electronic structure of active sites to reduce energy barriers but also reorganize interfacial water molecules into a strongly hydrogen-bonded network, significantly enhancing proton transfer efficiency. When implemented in a practical AEMWE, the system achieves 1.0 A cm^{-2} at 1.77 V and 80 °C while sustaining stable operation for 500 h, substantially outperforming noble-metal benchmarks. Beyond offering a high-performance catalyst system, this work provides valuable mechanistic understanding of reconstruction-driven catalysis and interfacial water regulation, offering guidance for the rational design of advanced electrocatalysts toward sustainable hydrogen production.

DECLARATIONS

Authors' contributions

Writing - original draft, investigation, formal analysis: Zhang, J.; Li, J.
Investigation, methodology: Zhang, J.; Han, M.; Xia, S.

Writing- review & editing, formal analysis: Wang, Y.; Luan, C.; Yu, C.
Reviewed the final manuscript, supervision: Wu, Y.; Zhang, W.
All authors contributed to the conceptualization of this work.

Availability of data and materials

The data supporting the findings of this study are available within the article and its Supplementary Materials. Additional data are available from the corresponding author upon reasonable request.

AI and AI-assisted tools statement

Not applicable.

Financial support and sponsorship

This work is supported by the National Natural Science Foundation of China (52202226, 52172293, and 52402358), Anhui Natural Science Foundation (2208085MC48), the Central Universities (JZ2024HGTG0293, PA2025GDSK0052, and JZ2025HGTB0213), 2024 Team Project under the Anhui Provincial Jianghuai Talent Cultivation Program, and the 111 Project (B18018).

Conflicts of interest

All authors declared that there are no conflicts of interest.

Ethical approval and consent to participate

Not applicable.

Consent for publication

Not applicable.

Supplementary Materials

Supplementary Materials

REFERENCES

1. Qiu, C.; Sellers, C.; Wu, Z.; et al. Low-iridium stabilized ruthenium oxide anode catalyst for durable proton-exchange membrane water electrolysis. *Nat. Nanotechnol.* **2025**, *20*, 1787-95. DOI
2. Yang, C.; Gao, Y.; Xing, Z.; et al. Bioinspired Sulfo oxygen bridges optimize interfacial water structure for enhanced hydrogen oxidation and evolution reactions. *Nat. Commun.* **2025**, *16*, 6459. DOI PubMed PMC
3. Li, P.; Jiang, Y.; Hu, Y.; et al. Hydrogen bond network connectivity in the electric double layer dominates the kinetic pH effect in hydrogen electrocatalysis on Pt. *Nat. Catal.* **2022**, *5*, 900-11. DOI
4. Gao, X.; Chen, Y.; Wang, Y.; et al. Next-generation green hydrogen: progress and perspective from electricity, catalyst to electrolyte in electrocatalytic water splitting. *Nano. Micro. Lett.* **2024**, *16*, 237. DOI PubMed PMC
5. Sadeghi, E.; Chamani, S.; Peighambardoust, N. S.; Aydemir, U. Unveiling the potential of metal diborides for electrocatalytic water splitting: a comprehensive review. *Energy. Environ. Mater.* **2025**, *8*, e12873. DOI
6. Shah MSA, Jang GY, Zhang K, Park JH. Transition metal carbide-based nanostructures for electrochemical hydrogen and oxygen evolution reactions. *EcoEnergy* **2023**, *1*, 344-74. DOI
7. Jia, X.; Zhou, Z.; Liu, F.; et al. Closed-loop framework for discovering stable and low-cost bifunctional metal oxide catalysts for efficient electrocatalytic water splitting in acid. *J. Am. Chem. Soc.* **2025**, *147*, 22642-54. DOI
8. Jeong, Y.; Naik, S. S.; Theerthagiri, J.; et al. Manifolding surface sites of compositional CoPd alloys via pulsed laser for hydrazine oxidation-assisted energy-saving electrolyzer: activity origin and mechanism discovery. *Chem. Eng. J.* **2023**, *470*, 144034. DOI
9. Hai, G.; Xue, X.; Wu, Z.; Zhang, C.; Liu, X.; Huang, X. High-throughput calculation-based rational design of Fe-doped MoS_2 nanosheets for electrocatalytic pH-universal overall water splitting. *J. Energy. Chem.* **2024**, *91*, 194-202. DOI
10. Tripathi, P.; Singh, D.; Pathak, A.; Verma, A. K.; Sinha, A. S. K.; Singh, S. Engineering MoS_2-based electrocatalysts for water splitting: a comprehensive review of doping, heterostructures, and support integration strategies. *J. Mater. Chem. A.* **2025**, *13*, 39603-59. DOI

11. Wei, R.; Liao, M.; Sun, L.; et al. Opposite electron transfer induced high valence Mo sites for boosting the water splitting performance of Ir atoms. *ACS. Appl. Mater. Interfaces.* **2024**, *16*, 7141-51. DOI
12. Yang, L.; Yuan, X.; Chen, C.; Wang, Q.; Liang, W.; Song, R. Rational design of MoS_2@M (M=Sn, Cu, Ni, Co) hybrid nanostructures for enhanced electrocatalytic hydrogen evolution reaction. *Mater. Chem. Phys.* **2024**, *318*, 129234. DOI
13. Wang, X.; Yang, C.; Zhang, Y.; et al. Medium-entropy alloy MoCoCu-P as an efficient bifunctional catalyst for water splitting. *J. Alloys. Compd.* **2024**, *988*, 174332. DOI
14. Fu, Y.; Wang, J.; Ma, X.; et al. Ion-exchange strategy for fabricating highly dispersed Co-MoS_2 on N-doped graphene for efficient bifunctional electrocatalytic water splitting. *Int. J. Hydrogen. Energy.* **2024**, *59*, 116-24. DOI
15. Gupta, J.; Das, D.; Borse, P. H.; Sarada, B. V. *In situ* Pd-doped MoS_2 nanosheets as an HER electrocatalyst for enhanced electrocatalytic water splitting. *Sustain. Energy. Fuels.* **2024**, *8*, 1526-39. DOI
16. Min, X.; Wang, L.; Liu, H.; et al. Molybdenum and fluorine co-doping induces lattice oxygen activation in Ni-Fe spinel oxides for enhanced oxygen evolution. *Energy. Mater.* **2026**, *6*, 600014. DOI
17. Lin, G.; Dong, A.; Li, Z.; et al. An interlayer anchored NiMo/MoO_2 electrocatalyst for hydrogen evolution reaction in anion exchange membrane water electrolysis at high current density. *Adv. Mater.* **2025**, *37*, 2507525. DOI
18. Gultom, N. S.; Li, C.; Kuo, D.; Silitonga, M. Z. Multiphase Fe-doped Ni_3S_2/MoO_x electrocatalyst prepared by facile one-step hydrothermal for full-cell water splitting: Effect of Mo on physical and electrochemical properties. *Appl. Catal. B. Environ. Energy.* **2024**, *353*, 124100. DOI
19. Wen, H.; Zhao, Y.; Zhang, H.; Wan-Me, Z.; Wan, X.; Xie, Y. Construction of an advanced MoS_2/MoO_3/NiFe-LDH/NF heterostructure catalyst toward boosting efficient alkaline oxygen evolution reaction. *Catal. Sci. Technol.* **2025**, *15*, 3871-7. DOI
20. Li, Y.; Wang, C.; Cui, M.; Xiong, J.; Mi, L.; Chen, S. Heterostructured MoO_2@MoS_2@Co_9S_8 nanorods as high efficiency bifunctional electrocatalyst for overall water splitting. *Appl. Surf. Sci.* **2021**, *543*, 148804. DOI
21. Wang, S.; Chen, S.; Wen, C.; et al. Nitrogen-doped MoO_2/Cu heterojunction electrocatalyst for highly efficient alkaline hydrogen evolution reaction. *Int. J. Hydrogen. Energy.* **2024**, *66*, 103-9. DOI
22. Sood, P.; Krishankant; Bagdwal, H.; et al. Polyoxometalate-derived Cu-MoO_2 nanosheets as electrocatalysts for enhanced acidic water oxidation. *ACS. Appl. Nano. Mater.* **2023**, *7*, 69-76. DOI
23. Teli, A. M.; Mishra, R. K.; Shin, J. C.; Jeon, W. Exploring the capability of Cu-MoS_2 catalysts for use in electrocatalytic overall water splitting. *Micromachines* **2024**, *15*, 876. DOI PubMed PMC
24. Lin, T.; Xu, R.; Hu, Y.; Wang, J.; Liu, Y.; Zhou, W. The dependence of electrocatalytic HER activity of decorated MoS_2 with Cu nanoclusters. *Surf. Interf.* **2024**, *46*, 104095. DOI
25. Ren, Z.; Wang, S.; Yu, J.; Mao, F.; Wang, K.; Wu, H. Cu/MoO_2 Schottky heterojunction derived from a new designed POMOFs in-situ as high efficient electrocatalysts for hydrogen evolution reaction in universal-pH electrolytes and seawater. *Chem. Eng. J.* **2023**, *470*, 144107. DOI
26. Ilyas, T.; Raziq, F.; Ali, S.; et al. Facile synthesis of MoS_2/Cu as trifunctional catalyst for electrochemical overall water splitting and photocatalytic CO_2 conversion. *Mater. Des.* **2021**, *204*, 109674. DOI
27. Zhao, Y.; Yang, Z.; Zhang, Y.; et al. Cu_2O decorated with cocatalyst MoS_2 for solar hydrogen production with enhanced efficiency under visible light. *J. Phys. Chem. C.* **2014**, *118*, 14238-45. DOI
28. Yang, L.; Yuan, X.; Song, R.; Liang, W. Cu doped MoS_2 nanosheets/NiS_2 nanowires heterogeneous structure for enhanced hydrogen evolution reaction. *J. Phys. Chem. Solids.* **2023**, *181*, 111540. DOI
29. Xu, G.; Geng, S. Copper-triggered adjacent S sites activating for enhancing the hydrogen evolution reaction in acid media. *J. Electroanal. Chem.* **2025**, *994*, 119276. DOI
30. Li, Z.; Yan, X.; He, D.; et al. Manipulating coordination structures of mixed-valence copper single atoms on 1T-MoS_2 for efficient hydrogen evolution. *ACS. Catal.* **2022**, *12*, 7687-95. DOI
31. Mi, Z.; Wei, F.; Yang, K.; et al. A bidentate hydrogen-bond molecular vise activates interfacial water for universal hydrogen electrocatalysis. *J. Am. Chem. Soc.* **2026**, *148*, 10388-95. DOI
32. Zhong, L.; Li, Y.; Zheng, L.; et al. Cu-mediated proximal electronic engineering in Ni/MoO_2 heterostructures for industrial alkaline hydrogen evolution. *Chem. Eng. J.* **2025**, *526*, 170806. DOI
33. Theerthagiri, J.; Karuppasamy, K.; Lee, S. J.; et al. Fundamentals and comprehensive insights on pulsed laser synthesis of advanced materials for diverse photo- and electrocatalytic applications. *Light. Sci. Appl.* **2022**, *11*, 250. DOI PubMed PMC
34. Al-Salihy, A.; Hu, J.; Liang, C.; Salah, A.; Bahgat, Radwan. A.; Xu, P. Optimizing surface structure with Cu nanodots-decorated $NiMoO_4$ nanostructures to enhance electrocatalytic water splitting. *Int. J. Hydrogen. Energy.* **2025**, *119*, 82-94. DOI

35. Chai, X.; Yuan, C.; Gao, R. T.; Wang, L. MoO_x/CoMo on Cu nanowires as an efficiently bifunctional electrocatalyst for overall water splitting. *ChemCatChem* **2024**, *16*, e202400582. DOI
36. Kühne, T. D.; Iannuzzi, M.; Del, Ben. M.; et al. CP2K: an electronic structure and molecular dynamics software package - Quickstep: efficient and accurate electronic structure calculations. *J. Chem. Phys.* **2020**, *152*, 194103. DOI
37. Hutter, J.; Iannuzzi, M.; Schiffmann, F.; Vandevondele, J. cp2k: atomistic simulations of condensed matter systems. *WIREs. Comput. Mol. Sci.* **2013**, *4*, 15-25. DOI
38. Lu, T.; Chen, F. Multiwfn: a multifunctional wavefunction analyzer. *J. Comput. Chem.* **2011**, *33*, 580-92. DOI
39. Lu, T. A comprehensive electron wavefunction analysis toolbox for chemists, Multiwfn. *J. Chem. Phys.* **2024**, *161*, 082503. DOI
40. Perdew, J. P.; Burke, K.; Ernzerhof, M. Generalized gradient approximation made simple. *Phys. Rev. Lett.* **1996**, *77*, 3865-8. DOI PubMed
41. Grimme, S.; Ehrlich, S.; Goerigk, L. Effect of the damping function in dispersion corrected density functional theory. *J. Comput. Chem.* **2011**, *32*, 1456-65. DOI PubMed
42. Goedecker, S.; Teter, M.; Hutter, J. Separable dual-space Gaussian pseudopotentials. *Phys. Rev. B.* **1996**, *54*, 1703-10. DOI
43. Lee, Y. J.; Park, S. K. Synergistically coupling of Ni-Fe LDH arrays with hollow Co-Mo sulfide nanotriangles for highly efficient overall water splitting. *Rare. Metals.* **2023**, *43*, 522-32. DOI
44. Liu, S.; Zhang, Z.; Dastafkan, K.; Shen, Y.; Zhao, C.; Wang, M. Yttrium-doped NiMo-MoO_2 heterostructure electrocatalysts for hydrogen production from alkaline seawater. *Nat. Commun.* **2025**, *16*, 773. DOI PubMed PMC
45. Dongre, S. S.; Kumar, R.; Paswan, B.; et al. Synergistic electrocatalytic activity unveiled: Cu-Mo bimetal sulfo-selenide nanocomposite for hydrogen evolution reaction. *Mater. Today. Sustain.* **2024**, *27*, 100894. DOI
46. Zhang, J.; Wang, Y.; Cui, J.; et al. Water-soluble defect-rich MoS_2 ultrathin nanosheets for enhanced hydrogen evolution. *J. Phys. Chem. Lett.* **2019**, *10*, 3282-9. DOI
47. Zhan, G.; Zhang, J.; Wang, Y.; et al. MoS_2 quantum dots decorated ultrathin NiO nanosheets for overall water splitting. *J. Colloid. Interface. Sci.* **2020**, *566*, 411-8. DOI
48. Liu, Q.; Fu, T.; Xiao, H.; et al. Constructing the Ni_4N/Ni_3N heterointerface of the bicontinuous Ni_4N/Ni_3N/NiO/CFs catalyst with pore connectivity effects for electrocatalytic hydrogen generation. *Carbon. Neutral.* **2025**, *4*, e70024. DOI
49. Zhang, B. J.; Chang, B.; Qiu, S. P.; et al. Two-dimensional bifunctional electrocatalyst (Mo-NiFe-LDH) with multilevel structure for highly efficient overall water splitting. *Rare. Metals.* **2024**, *43*, 2613-22. DOI
50. Zander, J.; Marschall, R. 1 min synthesis of phase pure nanocrystalline high-entropy sulfides for efficient water electrolysis. *EcoEnergy* **2025**, *3*, 482-98. DOI
51. Wang, R.; Sun, X.; Zhong, J.; Wu, S.; Wang, Q.; (ken), Ostrikov. K. Low-temperature plasma-assisted synthesis of iron and nitrogen co-doped CoFeP-N nanowires for high-efficiency electrocatalytic water splitting. *Appl. Catal. B. Environ. Energy.* **2024**, *352*, 124027. DOI
52. Tian, F.; Geng, S.; Li, M.; et al. Synergetic oxidized Mg and Mo sites on amorphous Ru metallene boost hydrogen evolution electrocatalysis. *Adv. Mater.* **2025**, *37*, 2501230. DOI
53. Zhu, S.; Qin, X.; Yao, Y.; Shao, M. pH-dependent hydrogen and water binding energies on platinum surfaces as directly probed through surface-enhanced infrared absorption spectroscopy. *J. Am. Chem. Soc.* **2020**, *142*, 8748-54. DOI PubMed
54. Liu, G.; Song, C.; Li, X.; et al. Defect-rich FeCoNiMnRu high-entropy alloys with activated interfacial water for boosting alkaline water/seawater hydrogen evolution. *Chem. Eng. J.* **2025**, *509*, 161070. DOI
55. Li, P.; Jiang, Y.; Men, Y.; Jiao, Y.; Chen, S. Kinetic cation effect in alkaline hydrogen electrocatalysis and double layer proton transfer. *Nat. Commun.* **2025**, *16*, 1844. DOI PubMed PMC
56. Jin, D.; Qiao, F.; Zhou, Y.; et al. Cu/Mo_2C synthesized through anderson-type polyoxometalates modulate interfacial water structure to achieve hydrogen evolution at high current density. *Nano. Res.* **2023**, *17*, 2546-54. DOI
57. Men, Y.; Men, X.; Li, P.; et al. Cation-driven modulation of interfacial solvation structures for enhanced alkaline hydrogen oxidation kinetics. *J. Am. Chem. Soc.* **2025**, *147*, 21672-85. DOI
58. Feng, M.; Tang, Y.; Li, Z.; et al. Differentiated modulating the electronic structure of NiFe@Ni/Fe-MnO_x via phase transformation engineering to synergy promote bifunctional water splitting reactions. *Small* **2025**, *21*, 2410752. DOI
59. Ma, W.; Zhang, Y.; Hu, L.; Lv, X.; Dang, J. Dynamic restructuring of asymmetric built-in electric field catalysts facilitates the efficient water splitting. *Adv. Funct. Mater.* **2024**, *35*, 2422734. DOI
60. Nguyen, T. H.; Tran, P. K. L.; Tran, D. T.; Dinh, V. A.; Kim, N. H.; Lee, J. H. Ru-Ru_2P hetero-cluster promoted V_2CT_x sheets-based electrocatalyst enables industrial-level AEM water electrolysis. *Appl. Catal. B. Environ.* **2024**, *343*, 123517. DOI
61. Long, Y.; Zhao, S.; Wang, L.; et al. Regulating high electron spin state in Co_3S_4 for enhanced water splitting. *ACS. Catal.* **2025**, *15*, 9845-55. DOI